A comparison framework for breathing motion estimation methods from 4D imaging

David Sarrut^{a,b}, Bertrand Delhay^b, Pierre-Frédéric Villard^c, Vlad Boldea^{a,c}, Michael Beuve^c and Patrick Clarysse^b

Abstract—Motion estimation is an important issue in radiation therapy of moving organs. In particular, motion estimates from 4D imaging can be used to compute the distribution of absorbed dose during the therapeutic irradiation. We propose a strategy and criteria incorporating spatio-temporal information to evaluate the accuracy of model based methods capturing breathing motion from 4D CT images. This evaluation relies on the identification and tracking of landmarks on the 4D CT images by medical experts. Three different experts selected more than 500 landmarks within 4D CT images of lungs for three patients. Landmark tracking was performed at 4 instants of the expiration phase. Two metrics are proposed to evaluate the tracking performance of motion-estimation models. The first metric cumulates over the 4 instants the errors on landmark location by the models. The second metric integrates the error over a time interval according to an *a priori* breathing model for the landmark spatio-temporal trajectory. This latter metric better takes into account the dynamics of the motion. A second aim of the study was to estimate the impact of considering several phases of the respiratory cycle as compared to using only the extreme phases (end-inspiration and end-expiration). The accuracy of three motion estimation models (two image registration based methods and a biomechanical method), were compared through the proposed metrics and statistical tools. This study points out the interest of taking into account more frames for reliably tracking the respiratory motion.

Index Terms—deformable registration, validation, thorax, radiotherapy

I. INTRODUCTION

Accounting for organ motion due to breathing in lung cancer radiation treatment is an important challenge [1]. Reducing uncertainties on target position should result in decreasing irradiation of healthy lung areas and should allow tumor dose escalation, potentially leading to better outcome [2]. Several approaches are currently under investigation (breath-hold treatment, gating [3] ...) but all require patient-specific spatio-temporal information about movements and deformations induced by breathing. Ideally, treatment planning should not rely on 3D images only, but also on a patient-specific breathing thorax model, encompassing all mechanical and functional information available. Some data can be obtained from 4D CT imaging [4], but 4D images alone are not sufficient and should be associated with new image analysis tools such as motion estimators and anatomical structure tracking methods [5]. They can also be used to build a "4D model" composed of spatio-temporal trajectories of all volume elements in the thorax. Using such a model would make it possible to select the best way of managing organ motion for each patient and provide helpful information for planning real-time tracking and dose delivery.

For example, a motion margin can be defined in order to account for respiratory motion, leading to unnecessary irradiation of large volumes of normal tissues. Zhang et al. [6] have proposed to incorporate target motion into treatment optimization using the displacement vector fields at different breathing phases, based on patient 4D CT images; beam targeting is optimized according to the motion. Instructing the patient to breathe following a visually displayed guiding cycle potentially allows to spare larger volumes of normal tissue. Rietzel et al. [7] have delineated volumes of interest in each phase of a 4D CT dataset and used them to determine the maximal displacement of GTV[1] centroids. Using B-spline deformable registrations, they have tried to quantify the impact of respiratory motion on generated dose distributions. The dose delivered to a given volume is directly related to the time of irradiation[2]. Therefore, motion of the tumors must be taken into account during the whole respiratory cycle. Brock et al. [8] have developed an approximation to modulate the weight of dose calculations from the exhale toward the inhale model as breathing progresses and using time weights obtained via fluoroscopy on a given population of patients. Keall et al. [5] have extended this concept to DMLC-based (Dynamic Multi-Leaf Collimator[3]) respiratory motion tracking. They have used deformable image registration to automatically transfer contours defined on the peak-inhale CT scan to other respiratory phase CT images. Dose distributions at each phase were then computed with phase-adapted MLC-defined beam, then mapped back to a reference CT image using estimated deformation fields.

(a) M. Sarrut and M. Boldea are with the Léon Bérard cancer center, 28 rue Laennec, 69373, Lyon, France. Email: David.Sarrut@creatis.insa-lyon.fr

(b) M. Sarrut, M. Delhay and M. Clarysse are with CREATIS (UMR CNRS 5220, Unité INSERM U630) INSA - Bâtiment Blaise Pascal, 7 avenue Jean Capelle, 69621 Villeurbanne cedex, France

(c) M. Villard, M. Boldea and M. Beuve are with Université de Lyon, Lyon, F-69003, France ; université Lyon 1, Lyon, F-69003, France ; CNRS, UMR 5205, LIRIS, Laboratoire d'InfoRmatique en Images et Systèmes d'information, Villeurbanne, F69622, France

---

[1]Gross Tumor Volume

[2]Dynamic aspect of IMRT (*Intensity Modulated Radiation Therapy*) may induce more complex behavior, but is not considered here

[3]In radiation therapy, a Multi-Leaf Collimator (MLC) is a device used for delimiting the radiation beam. It generally consists of two pairs of opposite jaws reshaping beams to a square or rectangular cross-section. Dynamic MLC supposes that leafs can move during irradiation.

Breathing motion tracking has been a fundamental element in these recent studies and must therefore be validated. Time-related issues must also be taken into account. A major challenge in deformable motion estimation is the validation of the resulting deformation fields. Today, contrary to the rigid motion case [9]–[11], there are few evaluation standards for deformable motion estimation. A tentative evaluation framework has been proposed by Hellier et al. [12] which focuses on the deformable registration of the brains of different individuals. In the present paper, our goal was to quantitatively compare motion estimators by taking into account the temporal aspects of the observed motions. Our clinical motivation was related to the use of deformable motion estimators with 4D scans to simulate radiation dose delivery inside moving and deforming organs for given irradiation configurations. We propose a framework and criteria incorporating temporal information to evaluate the accuracy of motion estimation methods for the purpose of compensating for breathing motion in 4D CT images. The proposed framework will be illustrated with the evaluation of three different motion estimation methods in terms of accuracy.

The paper is organized as follows. Section II briefly presents the experimental 4D CT data used in the study. Our approach for the evaluation of motion tracking methods in 4D CT sequences is based on landmark location estimation. Section III-A and III-B explains how the landmarks have been selected and tracked by medical experts. Then, two error criteria to evaluate the accuracy of landmark location estimated by motion tracking methods are introduced. The first one is the generalization of the conventional TRE metric to the tracking in successive images (section III-C). The second one, takes into account the temporal nature of the motion and is presented in III-D. Section IV describes three motion tracking methods compared using the proposed strategy. Results are presented in sections V. Section VI compares the behavior of the motion tracking methods and discuss the respective properties of the two metrics.

II. MATERIALS

This study considered as input data thoracic 4D CT sequences from patients with non small-cell lung cancer (NSCLC). 4D images were acquired according to a recent protocol similar to the one described in [13], using a "cine" scanning protocol: multiple image acquisitions were performed along the cranio-caudal direction at a time interval greater than the average respiratory cycle. The acquisition was repeated until the prescribed volume was completely scanned. During the entire acquisition, an external respiratory signal, generated with the Real-Time Position Management (RPM) Respiratory Gating System (from Varian Medical Systems, Palo Alto, CA), was recorded. The signal was then used to sort data into respiratory phases by selecting, for each slice position and for each phase, the closest image. The resulting 4D images were composed of ten 3D images covering a respiratory cycle from the end of normal inspiration to the end of normal expiration.

In this study, we focused on the *expiration part* of the respiratory cycle (six out of ten frames, including extreme phases).

The number of exploitable frames varies from one dataset to the other and the common maximum number in our series was four out of six. We thus decided to consider four images: two extreme images (denoted I_I for end-inspiration and I_E for end-expiration) and two intermediate images denoted I_1 and I_2, corresponding to intermediate lung volumes. For some reasons (too rapid patient breath, inaccuracy of the external respiratory signal), selected data at a given phase and slice position may not be consistent. Hence, the corresponding 3D images presented some misaligned slices, generally around the diaphragm (see Figure 1). Some other (less frequent) artifacts were probably due to patient movement during scanning.

At the time when the acquisitions were performed according to this protocol, 3 patient datasets (referred to as patient 1, 2 and 3 in the sequel) were found exploitable. Image size was 512×512 pixels, with 88, 115, 120 slices for patients 1, 2 and 3, respectively. In all images, pixel size was $0.97 \times 0.97 \, mm^2$ and slice thickness $2.5 \, mm$. All tumors were located in the lower part of the right lung. The tumor volume was approximately 160, 165 and $37 \, cm^3$ in patients 1, 2 and 3, respectively.

Note also that the same phase can correspond to different lung volume percentages in different patients depending on each patient's breathing pattern. Approximated lung volumes were computed (see Tab. I) by automated segmentation using thresholding and morphological operations as described in [14]. Maximal displacements close to the diaphragm were estimated to: $23 \, mm$, $25 \, mm$ and $17 \, mm$ for patients 1, 2 and 3, respectively. We want to emphasize that the use of 4D CT images is relatively new in the field of radiation therapy and that, although the technique has already been used in several clinical studies, it is still under developpement.

TABLE I
LUNG VOLUMES (IN cm^3 AND IN % OF THE DIFFERENCE BETWEEN I_E AND I_I) FOR ALL IMAGES.

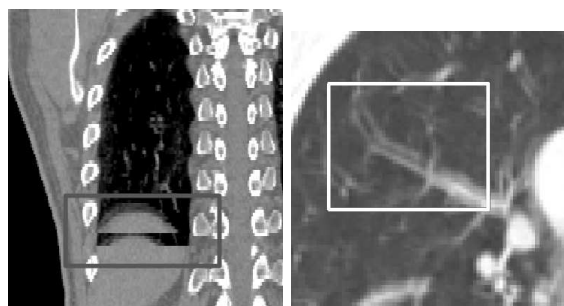| Images	$patient1$	$patient2$	$patient3$
I_I	5181 (100%)	3214 (100%)	3121 (100%)
I_1	5004 (50%)	2981 (49%)	2897 (47%)
I_2	4692 (44%)	2880 (27%)	2797 (24%)
I_E	4315 (0%)	2755 (0%)	2696 (0%)

Fig. 1. Examples of image artifacts. (Left) several slices were missing at the given temporal phase. (Right) Blurred structures inside the lung due to unforeseen movement.

III. METHODS

Criteria permitting to evaluate and compare breathing motion estimators are proposed. They rely on the comparison of landmark locations obtained by manual reference selection (see next sub-section) and landmark locations obtained by applying deformation fields obtained using automated motion estimation methods. Three methods (m_1, m_2 and m_3) will be described in section IV to illustrate the proposed evaluation framework. For comparison purpose, we found it important to compare results obtained by these methods against the situation where no compensation was performed (noted m_0). Methods evaluation was based on two spatio-temporal distances between reference and observed trajectories, and distance to direct straight line trajectories. Section III-A and III-B describes landmark selection and tracking. Section III-C and III-D present the two evaluation approaches.

A. Landmark selection

A set of anatomical landmarks were selected and labeled inside the lungs in the reference image I_I of each of the three patients, by three medical experts. The instructions were to select salient anatomical features: each landmark should be undoubtedly identifiable and labeled with a descriptive name allowing other experts to find it. Examples of salient points are : carina, calcified nodules, culmen-lingula junction, specific branch of pulmonary arteries, apical pulmonary vein of the upper lobe, etc (see Fig. 2). Actually, there might be some degree of statistical dependence between landmark point locations. In order to limit the impact of this dependence onto the statistical analysis, we asked the experts to select points distributed as evenly as possible all over the lungs (left/right lung, upper/lower and central/peripheral parts of the lungs). The experts were also instructed to identify as many landmarks as possible with a minimum of 20. However, some experts extracted twice as many landmarks as the others. Up to 27 points were selected in Patient 1, 41 in Patient 2 and 56 in Patient 3.

The tracking of initial landmarks across the following frames was performed by all the experts. They were not authorized to see other experts' results so as not to bias the selection. Finally, all inputs were averaged to obtain mean landmark locations. Let $\mathbf{p}_i^{e,k}$ denote the location of the kth landmark in image i (with $i \in \{I, 1, 2, E\}$, I and E corresponding to end-inspiration and end-expiration, respectively), selected by expert e. The three point locations issued from the different expert selections were averaged to define pseudo-ground truth landmarks denoted by :

$$\mathbf{q}_i^k = \frac{1}{3}\sum_e \mathbf{p}_i^{e,k} \qquad (1)$$

except for the reference image I_I in which $\mathbf{q}_I^k$ was the result of a unique selection. In order to estimate the inter-expert variability associated with manual identification of anatomical landmarks, we computed the standard deviation of the distances between all $\mathbf{q}_i^k$ and $\mathbf{p}_i^{e,k}$ values.
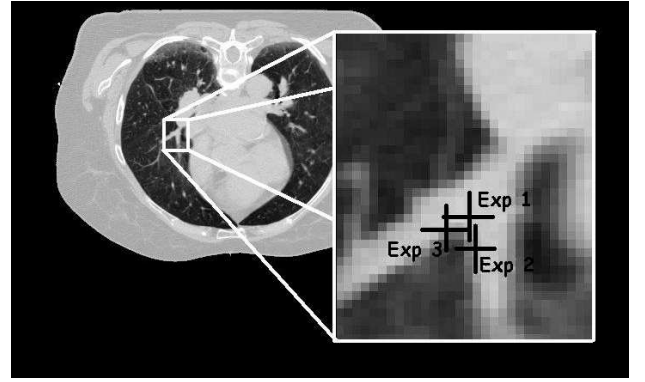

Fig. 2. Example of landmark selection by the three experts. The mean position corresponds to the pseudo-ground truth landmark. In this example, the three positions lie on the same slice but this was not always the case.

B. Landmark tracking

Landmark motion is represented by a trajectory. A physical point at a given reference time is identified by its geometrical position: $\mathbf{x}_0 = (x_0, y_0, z_0)$. The mapping $\mathbf{x} = \phi(\mathbf{x}_0, t)$ stands for the geometrical position of the same physical point at time t. ϕ is the function which maps the physical point $\mathbf{x}_0$ from time t_0 to time t. By definition, $\phi(\mathbf{x}_0, t_0) = \mathbf{x}_0$. The geometrical positions of the landmarks are expressed for discrete times of interest according to the previous definitions. $\mathbf{q}_I^k$ denotes the position of the kth landmark in the reference image $\mathbf{I}_I$. We have the following relation:

$$\mathbf{q}_i^k = \phi(\mathbf{q}_I^k, t_i) \qquad (2)$$

where $\phi(\mathbf{x}, t_i)$ maps every geometrical point $\mathbf{x}$ from reference time t_I to time t_i (with $i \in \{1, 2, E\}$).

In section IV, we will introduce examples of methods allowing to automatically estimate the displacement of the landmarks. For the three patient datasets, each method will be used to estimate the transformation $\tilde{\phi}$ between all images in the sequence (ie. I_1, I_2, I_E) and the reference end-inhalation image I_I (see Fig. 3). In the following, we will denote $\tilde{\phi}_i$ the estimated function which maps image I_I to image I_i.

C. Punctual accuracy analysis

The first criterion to assess the accuracy of the motion estimation methods is an extension of the Target Registration Error (TRE) proposed in [10]. Initially proposed for rigid motion, this criterion was extented to motion tracking of the sets of landmark points. Let us consider $\mathbf{q}_I^k$, the kth pseudo-ground truth landmark in the reference image I_I; its estimated geometrical location $\mathbf{r}_i^k$ in image I_i is calculated as $\mathbf{r}_i^k = \tilde{\phi}_i(\mathbf{q}_I^k)$. The difference between pseudo-ground truth landmark positions and estimated landmark positions is illustrated in Fig. 3. The TRE for the transformation between image I_I and image I_i is defined by:

$$TRE_i = \frac{1}{n}\sum_{k=1}^{n}\sqrt{(\mathbf{q}_i^k - \mathbf{r}_i^k)^2} \qquad (3)$$

where $n = 27$ for patient 1, $n = 41$ for patient 2 and $n = 56$ for patient 3. Error dispersion was represented using 'box
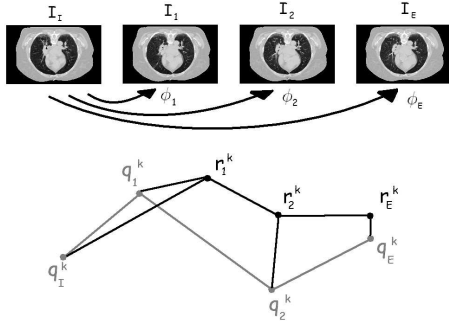
Fig. 3. (a) Transformations between all images in a sequence and the end-inspiration reference image I_I are estimated. (b) Expert (q_i^k) and estimated (r_i^k) landmark definitions.

and whiskers plots' [15] to highlight the median and mean of each sample, its spreading and possible outliers. Bland-Altman diagrams [16] were used to compare the motion estimation results obtained with the different methods. Finally, paired Student t-tests were performed to check whether two methods behaved equivalently or not, under the assumptions that the paired differences are independent and normally distributed (such assumptions were verified before applying the test).

D. Analysis of spatio-temporal trajectories

1) Respiratory cycle modeling: It is generally assumed that all the points in the volume reach their final position at the same time and that the temporal behavior along the trajectory is determined by a one dimensional breathing signal. Several models of breathing cycles have been proposed in the literature. We chose the one proposed by Lujan et al. [17] (Eq. 4) which models the dynamic breathing volume curve. It is based on a periodic but asymmetric function (more time spent at exhalation versus inhalation). In Eq. 4, V_0 is the volume at exhalation, b corresponds to the tidal volume (TV) which is the amount of air breathed in or out during normal respiration, $V_0 + b$ is the volume at inhalation, τ is the period of the breathing cycle, n is a parameter that determines the general shape (steepness or flatness) of the model, and φ is the starting phase of the breathing cycle (Fig. 4). Using the Lujan model, George et al. [18] have studied the correlation of respiratory motion traces between breathing cycles, based on 331 four-minute respiratory traces acquired from 24 lung cancer patients. They advocated the use of $n = 2$. We followed their suggestion in the present study. Of course, the period and magnitude of the motion due to breathing can vary, even over a short period of time. This model represents *a priori* knowledge of a conventional breathing cycle which will be incorporated into the validation procedure through the metrics introduced in the next section. Other models could also be considered. An illustration of the temporal position of each image in the test sequences according to this respiratory cycle modeling and the estimated volumes is given in Fig. 5 (see also Tab. I). The parameters for such a model can also be estimated using an external measurement system, such as the RPM.

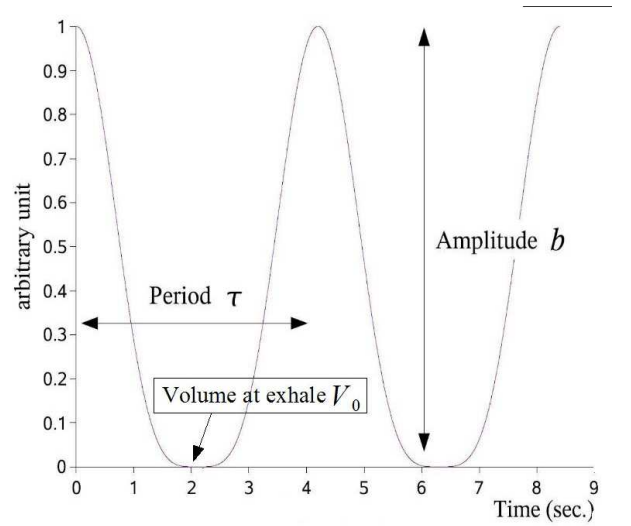$$V(t) = V_0 + b \cos^{2n}(\frac{\pi}{\tau}t - \varphi), \tag{4}$$

Fig. 4. Breathing cycle modeling proposed by Lujan et al. [17] ($n = 2$). See text for details.

2) Spatio-temporal localization error: The main drawback of the TRE metric is that it does not take into account the time spent at the main phases of a trajectory. According to the previously introduced breathing model (section III-D.1), material points move along their trajectory at variable speed (determined by the derivative of the volume curve V). In section A, we mentioned that the dose deposit was mainly related to the duration of irradiation. Thus, a global and more pertinent metric should take into account that more time is spent at the end-inspiration and end-expiration phases than between these extremes. In other words, estimation errors at an intermediate phase of the cycle should have lower weight than errors at extreme phases. This is the purpose of the following metric: for a given temporal interval $[t_a, t_b]$ of the respiratory cycle, we defined the Spatio-Temporal Error (STE) as:

$$STE_{t_a, t_b}(T_1, T_2) = \frac{1}{t_b - t_a} \int_{t_a}^{t_b} dist(T_1(s(t)), T_2(s(t)))dt \tag{5}$$

with $dist$ the Euclidean distance and $s(t)$ the curvilinear abscissa. T_1 and T_2 denoted two trajectories. Let T be a parametric trajectory (which defines the set of the different locations of a material point during its motion) defined by:

$$T : \quad [0, 1] \in \mathbb{R} \longrightarrow \mathbb{R}^3$$
$$s \longmapsto T(s) = \begin{bmatrix} x(s) \\ y(s) \\ z(s) \end{bmatrix} \tag{6}$$

where s is the normalized curvilinear abscissa of the trajectory. This abscissa is a function of time and denotes the curve length traveled between initial time t_a and time t. The relation between time t and abscissa s is thus defined by:

$$s : \quad [t_a, t_b] \in \mathbb{R} \longrightarrow [0, 1] \in \mathbb{R}$$
$$t \longmapsto s(t) \tag{7}$$

where s is a strictly increasing function. The breathing cycle *a priori* model is incorporated into the STE metrics through the volume evolution function $V(t)$ defined by Eq. (4). s is thus
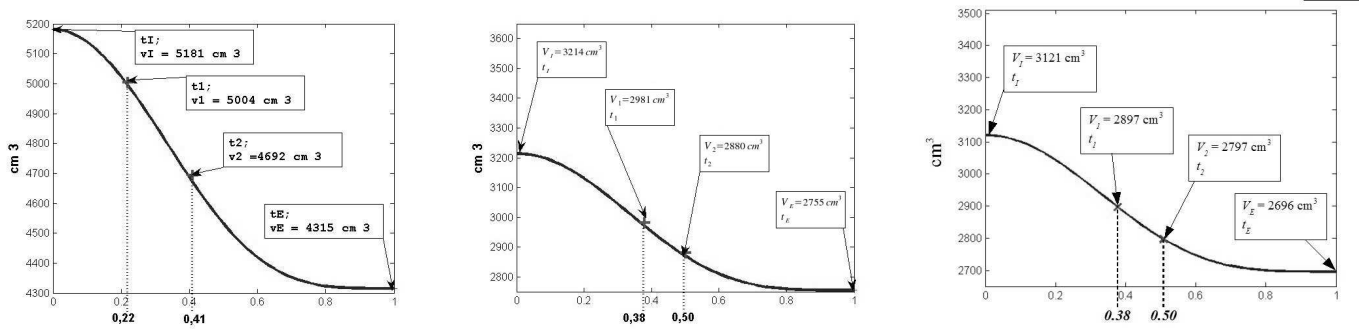
Fig. 5. Lung volume curves for the three patients during expiration. Values are indicated for the four time points estimated by the respiratory model introduced in section III-D.1. Left: $Patient1$; center: $Patient2$; right: $Patient3$.

expressed by $s(t) = (V(t) - V(t_a))/(V(t_b) - V(t_a))$. Fig. 6 illustrates the relation between respiratory cycle modeling $V(t)$ and the curvilinear abscissa. In this figure, the non-linear relation is compared to the linear case where $s(t) = (t - t_a)/(t_b - t_a)$. Practically, a constant time step δt corresponds to a non constant abscissa step such as $\delta s = \delta t \cdot ds/dt$ because of the relative breathing velocity ds/dt. The relation depends on the chosen breathing model. In our case, the trajectory samples are denser at phases close to the end-inspiration and end-expiration time points than at intermediate phases.
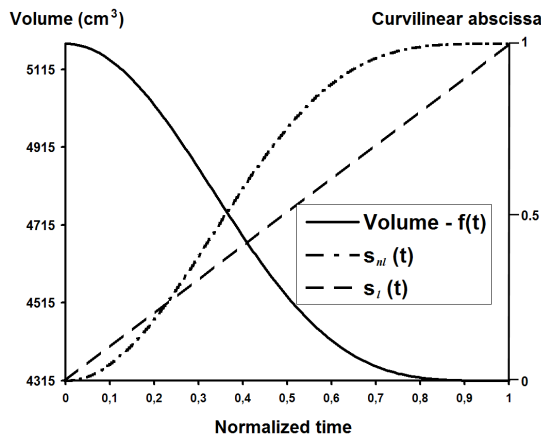

Fig. 6. Relation between the global breathing cycle model and the curvilinear abscissa s of the trajectories. The linear case $s_l(t) = t$ is represented by the dashed plot while the non linear case s_{nl} computed from the breathing cycle model (plain curve) is illustrated by the dash-dotted plot.

The parametric trajectories were chosen such that the elementary displacements are approximated by linear interpolation between each pair of phases considered, and the abscissa s traverses this piecewise-linear trajectory (see Fig. 3).

STE varies with the respiratory cycle model and the temporal spacing between images in the sequence (*i.e.*, the relative position at t_1 and t_2 during expiration phase). A STE value equal to x means that, over a given portion of the cycle (from t_a to t_b), using trajectory T_1 instead of T_2 leads to $x\,mm$ shift in average. In practice, Eq. 5 was computed by approximating the integral by a sum over a set (one hundred or more) of regularly temporally spaced samples. Figure 7 illustrates the distances between two trajectories computed with a linear and a non-linear relation between t and s.

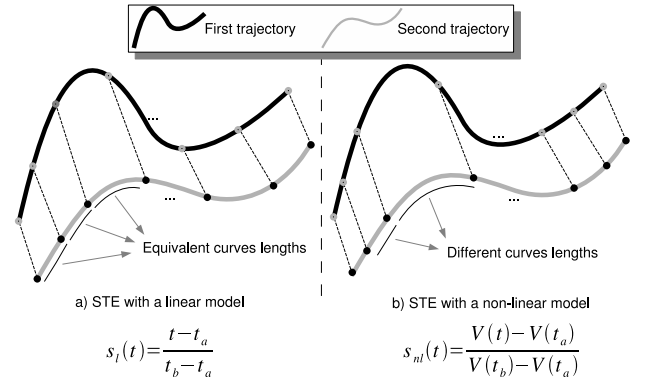

Fig. 7. Illustration of the STE criterion with a linear (left) and a non-linear (right) model.

3) Straight-linear and piecewise-linear direct trajectories: In order to clarify the different trajectories considered in the sequel, we introduced a set of acronyms whose meaning is illustrated in figure 8.

- **SRT** denotes the *Straight-linear Reference Trajectory*, that is the rectilinear trajectory obtained when directly connecting the points defined by the experts at the beginning and the end of expiration.
- **SET** stands for the *Straight-linear Estimated Trajectory*, the rectilinear trajectory obtained when directly connecting the position of a landmark extracted from the image taken at the beginning of expiration to the estimated corresponding point by a given method at the end of expiration.
- **PRT** corresponds to the *Piecewise-linear Reference Trajectory*, piecewise linear trajectory obtained when connecting the reference points issued from all the time points.
- **PET** denotes the *Piecewise-linear Estimated Trajectory*, the piecewise linear trajectory obtained when connecting the estimated points issued from all the time points.

IV. EXAMPLES OF MOTION ESTIMATORS EVALUATED IN OUR FRAMEWORK

In order to illustrate the use of this evaluation framework, we selected and compared three available motion estimation methods. The literature on motion estimation methods is abundant. One approach is to seek for a geometric transformation
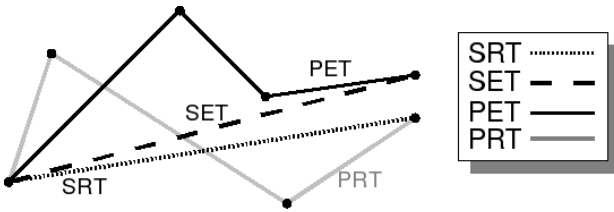
Fig. 8. Definition of Straight-Linear/Piecewise-Linear Reference/Estimated Trajectories.

between two consecutive images in a sequence. This process is known as image registration and two of the three methods are based on this concept. Image registration algorithms are currently described as the combination of several components: a feature space, a similarity measure, a transformation model and an optimization algorithm [19]–[21]. The goal is to find an optimal transformation that leads to maximum similarity (or minimum distance) between a reference image and a deformable floating image. Numerous methods have been proposed. Feature-based methods use landmark points [22], [23], organs contours [24], [25] or segmented surfaces to drive the transformation search. Intensity-based methods often refer to optical-flow like methods [22], [26], [27]. In this case, image similarity is defined as a statistical measure between the intensity (gray-levels) distributions of the two images, and deformable fields are the result of the optimization of a function establishing a tradeoff between image similarity and deformation smoothness. Another approach relies on biomechanical models [28]–[30] which do not explicitly use a similarity measure. Instead, they simulate organ deformation based on both physical material properties and constraints given by the initial and final states of the organs. They are usually based on the Finite-Element Method (FEM) and use physically-based equations (elastic model for example) to simulate individual organ deformation (represented by triangular meshes for surface-based models or tetrahedral meshes for volume-based models). The individual material properties of each organ have to be described, with parameters such as Young's modulus and Poisson's ratio.

In order to illustrate our evaluation framework, we considered the three following motion estimation methods: m_1 is a bi-pyramidal free form deformation method, m_2 is an optimized optical flow method and m_3 is a biomechanical method. These methods constitute rather conceptually different approaches to the problem of motion estimation. While m_1 is a parametric registration-based method, m_2 is a non-parametric one, and m_3 is based on an *a priori* physiological model of the lung dynamics. The three methods are therefore representative of different categories of motion estimation methods and good candidates to illustrate the proposed comparison techniques and metrics. The three methods are described hereafter. Let I_1 and I_2 be two images to be registered. We denote by $\mathbf{u}(\mathbf{x})$ the displacement of a point $\mathbf{x}$ and by $\phi(\mathbf{x}) = \mathbf{x} + \mathbf{u}(\mathbf{x})$, the deformation.

A. Method m_1 : bi-pyramidal free form deformation-based image registration

The non-rigid transformation is modeled using multi-level free form deformations [31], [32]. The basic idea of the free form deformation is to warp an object (a 3D image in the present case) by moving an underlying set of control points distributed over a regular grid [33], [34] (the sets of control points and the landmarks defined in section III-A are strictly uncorrelated). An interpolation function at each node of the grid is used to recover the final spatial continuous transformation. At any point $\mathbf{x}$, the deformation is computed by:

$$\phi(\mathbf{x}) = \mathbf{x'} = \mathbf{x} + \sum_{j \in J} \mathbf{Q}^j B_j(\mathbf{x}) \qquad (8)$$

where $J \in \mathbb{Z}^d$ defines the set of spatial parameter values, $\mathbf{Q}^j$ is a vector which contains the parameters of the transformation to be estimated (i.e. displacements of the control points) and $\mathbf{B}_j$ is a tensorial product of interpolation functions. We chose cubic B-Spline functions which are recognized to be the best choice in terms of computational efficiency, good approximation properties, and implicit smoothness (minimum curvature property) [35]. Cubic B-Spline functions have a limited support, and are C^3 continuous. Thus, the influence of each control point is local and the final motion field is continuous. If we consider that the object to deform belongs to the $\mathbb{R}^d$ space and that the warping grid size is N, the transformation is thus defined by $d \times N^d$ parameters.

The algorithm relies on a bi-pyramidal formulation. In the first pyramid $\mathcal{P}_1$, a multiresolution decomposition of the original image $(I_m, I_{m-1}, ..., I_0)$ is stored, where each sub-resolution level I_{m-1} is obtained by first applying a low-pass Gaussian filter to the current image I_m, then decimating the number of pixels (or voxels). The second pyramid $\mathcal{P}_2$ allows for the multiscale decomposition of motion field $\mathbf{u}$ [35]–[37]. The final mapping function ϕ belongs to the Hilbert space of finite energy deformation fields and can be approximated with a set of multilevel functions. The multilevel formulation of the transformation is described in [38]. At the coarsest level, ϕ_0 is defined by a few parameters. Once a deformation field has been estimated for one level l of $\mathcal{P}_2$, the next level is initialized using a projection onto the finer space. The algorithm is organized as follows: first, the transformation parameters are estimated at the coarsest image resolution and transformation level. Then, the image resolution is increased without changing any parameter of the transformation and a new estimation is performed. Afterward, the transformation level increases and previous parameters are projected onto the new finer space. These steps are repeated until the final image resolution and transformation levels are reached. The sum of squared differences (SSD) similarity criterion is used:

$$SSD(I_1, I_2, \phi) = \int_{\mathbf{x} \in \Omega} (I_1(\mathbf{x}) - I_2(\phi(\mathbf{x})))^2 \qquad (9)$$

(with Ω the image overlapping domain). This criterion assumes the invariance of the material point brightness during

$$\nabla_Q SSD(I_1, I_2, \phi) = -2 \times \int_{\mathbf{x} \in \Omega} (I_1(\mathbf{x}) - I_2(\phi(\mathbf{x}))) \times \frac{\partial I_2(\phi(\mathbf{x}))}{\partial \mathbf{Q}} \tag{10}$$

motion which is reasonable in our monomodal case. The optimization is achieved through a gradient descent search based on the first derivative (Eq. 10) of the SSD similarity criterion, with respect to the parameters of the current transformation level.

$$\frac{\partial I_2(\phi(\mathbf{x}))}{\partial \mathbf{Q}} = \left. \frac{\partial I_2(\phi(\mathbf{x}))}{\partial \mathbf{x}} \right|_{\phi(\mathbf{x})} \times \left. \frac{\partial \phi}{\partial \mathbf{Q}} \right|_{\mathbf{x}} \tag{11}$$

In Eq. 11, the terms on the right are respectively the gradient of I_2 at point $\mathbf{x} = \phi(\mathbf{x})$ and the Jacobian of the transformation with respect to the parameters at point $\mathbf{x}$. At each iteration, the parameters of the current transformation level are updated according to:

$$\mathbf{Q}_{i+1} = \mathbf{Q}_i + \lambda \nabla_Q SSD(I_1, I_2, \phi) \tag{12}$$

where λ is the maximum step of the gradient descent algorithm. We developed a C++ multithreaded version of the algorithm where the region of interest of the reference image was split according to the number of available processors. This considerably reduced the computing time on SMP architectures.

B. Method m_2: optimized optical flow method

The method m_2 is described in details in [39]. It involved three main steps: (1) preprocessing step consisting of segmenting the 3D images into three regions labeled as air, patient and lung, (2) *a priori* lung density modification in order to take into account the density decrease due to inhalation, (3) dense optical-flow like deformable registration.

The intensity conservation assumption implies that an image point has the same intensity in the other image but at a different location. However, lung densities are known to decrease from exhalation to inhalation according to the quantity of inhaled air. Therefore, the second step of this method aimed at artificially changing the lung density of one image in order to be closer to the intensity conservation assumption. We called this method *A Priori Lung Density Modification* (APLDM) [39]. Deformable registration was achieved by optimizing of a criterion composed of the SSD (see Eq. 9) and a regularization measure by a steepest gradient descent algorithm. Previous works have shown that elastic and Gaussian regularizations lead to similar results for thorax CT images [39]–[41]. In this work, we considered Gaussian regularization [42]. Gradient ∇L of the SSD criterion was expressed as proposed by Pennec et al. [43] (Eq. 13), which limits the local displacement at each iteration according to a

maximum vector displacement α. This criterion is an approximation of a second order gradient descent of the SSD [44]. The iterative process is given by Eq. 14.

$$\mathbf{u}_{i+1}(\mathbf{x}) = G_\sigma(\mathbf{u}_i(\mathbf{x}) + \nabla L(\mathbf{x}, \mathbf{u}_i)) \tag{14}$$

$\mathbf{u}(\mathbf{x})$ denotes the displacement at point $\mathbf{x}$, $\nabla I_1(\mathbf{x})$ denotes the gradient of image I_1 at point $\mathbf{x}$, $\mathbf{u}_i$ denotes the displacement field at iteration i and $G_\sigma(.)$ denotes Gaussian kernel of variance $\sigma > 0$ (the higher the σ value the smoother the vector field). Gaussian filtering was performed using Deriche recursive Gaussian filter [45]. Images were previously resampled to an isotropic voxel's size of $2.5 \, mm^3$.

C. Method m_3: Biomechanical method

Various studies have analyzed organ motion with FEM methods. Some methods have been proposed to reproduce the lung behavior, such as the one by Grimal et al. [46] that was used to study thoracic impact injuries. In this work, biomechanical parameters were studied in depth but breathing motion was not included into the modeling. Other methods focused on the breathing motion [47]. We recently proposed to apply, as boundary conditions, a normal displacement field to the external lung surface extracted from I_E limited by the maximal displacement field of the surface extracted from I_I. The method proposed has been detailed in [48]. It is based on a biomechanical approach and aims at physically simulating the lung behavior with laws of continuous mechanics based on physiological and anatomical studies and solved by FEM methods.

a) Model: The mechanical model was composed of: 1 - A geometrical description of the lung which was discretized into small elements to constitute a mesh, 2 - Mechanical parameters to properly describe lung tissue behavior and 3- Boundary conditions to define the muscle actions allowing pulmonary motion. The initial state was obtained by lung surface mesh extraction from the CT images. The mesh was multi-level: 1- An external smooth mesh was obtained by a surface reconstruction method (Marching Cube) [49]. 2- This algorithm was extended to also provide an accurate tetrahedral mesh of the lung periphery [50]. 3- A bulk mesh was modeled by hexahedrons directly extracted from CT scan voxels for better convergence rate. The mechanical parameters, especially compliance, were issued from physiological measurements [51]. Compliance represents the ratio of air volume variation to the related air pressure variation. Each patient's data are linked to lung tissue elasticity, especially the Young modulus. The boundary conditions were derived from

$$\nabla L(\mathbf{x}, \mathbf{u}) = \frac{I_1(\mathbf{x}) - I_2(\mathbf{x} + \mathbf{u}(\mathbf{x}))}{||\nabla I_1(\mathbf{x})||^2 + \alpha^2 (I_1(\mathbf{x}) - I_2(\mathbf{x} + \mathbf{u}(\mathbf{x})))^2} \nabla I_1(\mathbf{x}) \tag{13}$$

mechanical pleura action [52]. We computed the boundary conditions by imposing surface displacements. The boundaries of the lungs were modeled with a mesh extracted from CT scan image I_2 representing the deformed state. A uniform normal pressure was applied around the rib cage and around the diaphragm areas to simulate the pleural elastic recoil pressure. Adding contact condition constraints to that boundary allowed either to block the displacement or to simulate the slipping skins. Figure 9 illustrates these constraints. Note that in one dataset, the upper part of the lungs was missing. Therefore, the model could not be applied directly. To overcome this problem, the missing part of the lung apex (only about $1.5\,cm$) was approximated with a semi-ellipsoid. The semi-axe lengths were manually set.
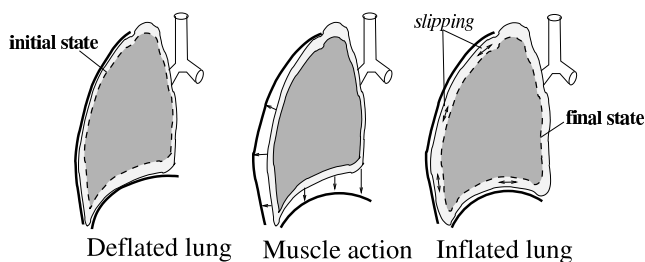

Fig. 9.   Boundary conditions defined by diaphragm and rib cage actions for the biomechanical model

b) Displacement estimation: The solution to the problem was achieved using the finite element method [53]. This numerical method consists in approaching the solution by a simple expression based on the discretization of the space into a mesh. In the present case, displacements U were estimated to minimize the residue R defined by:

$$R(U) = F - K(U).U = 0 \qquad (15)$$

where K is the stiffness matrix and F is the load vector. The term K expresses the rigidity of the lung. It depends both on mechanical parameters (Young modulus and Poisson's ratio) and on topological relationships between mesh nodes. The term F expresses the external forces applied to the lung, such as negative pressure. The displacement vector U represents the displacement of all the mesh nodes and allows to estimate the displacement in the whole lung by interpolation. The space of such displacements is a subspace of functions and minimizing the residue $R(U)$ is equivalent to finding the best approximation of the solution to laws of continuous mechanics describing the behavior of deformable solid under boundary condition stresses.

In our FEM approach, this non-linear problem was solved using the Newton-Raphson algorithm which is an iterative method based on the computation of the gradient and the second order gradient of $R(U)$. The displacements and strains were too large to assume that geometrical mesh changes would not influence the mechanical behavior. Therefore, we employed the iterative scheme presented in [54]. This method consists in readjusting the geometrical description at each load step in order to re-evaluate $K(U)$. To account for contact conditions, we calculated algebraic distances between the nodes of the lung surface and the triangles representing the target lung surface (end-inhalation). If a distance remained positive, a negative pressure was applied to the corresponding node. When this became zero or negative, a contact between the current and the target lung surface was assumed. In this case, a restoring force was applied to ensure that the node was pulled back to the target surface. The restoring force was set as normal at the surface in order to allow surface sliding.

Up to now, we have focused on the technical aspects of the method: convergence, biomechanical parameters influence and the interest of using a multi-layer mesh. The fact that the lungs are composed of different biological tissues was not taken into account in this study. As a consequence, mechanical properties were supposed to be uniform all over the lungs.

V. RESULTS

The two criteria TRE and STE, introduced in Eq. 3 and 5, were used to evaluate the motion estimates obtained by the three previously described methods applied to the 4D image sequences for the 3 patients presented in section II. Box and whiskers, Bland-Altman and Student paired t-tests analyses were derived for the two criteria. For methods m_1 and m_2, the resulting deformation field obtained between images I_I and I_1 was used as the starting deformation field for the subsequent registration (I_I to I_2), and so on. It allowed to save some initial iterations by starting closer to the solution. Method m_1 was run on a 1.5 Ghz Non Uniform Memory Access Multiprocessor SGI with 64Gb RAM, running Linux OS. The computation time for one iteration was related to the image resolution and the transformation level. For all the registrations, four image resolutions and four transformation levels were used with cubic B-Spline basis functions. The size of the regular grids were $5 \times 5 \times 5$, $7 \times 7 \times 7$, $11 \times 11 \times 11$ and $19 \times 19 \times 19$. Registration time, using 10 processors, ranged from 18 minutes (patient 1) to 22 minutes (patient 2). Method m_2 was run on a 2.8Ghz PC with 1Gb RAM running Linux OS. The computation time was about 1.5 seconds for one million voxels and for one iteration. Registration time ranged from 5 minutes to 9 minutes depending on the image size and the deformation to recover. Method m_3 was run on a 3.2Ghz PC. The computation time was about 2 minutes for a mesh composed of 7000 nodes and 20000 elements. Method m_3 was not applied to patient 3. Indeed, as the tumor was attached to the diaphragm, the lung surface was found difficult to extract reliably.

A. First criterion : TRE

Figure 10 displays the Box and Whiskers plots for TRE on the three patients (one line per patient). The three columns correspond to the three transformations ϕ_1, ϕ_2 and ϕ_E, respectively. Each plot shows the statistics for the four methods (m_0 stands for 'without registration', methods m_1, m_2, m_3 were described in section IV). Table II gives the TRE statistics obtained with all the methods. Bland-Altman analysis was performed on each pair of methods. Only two representative plots are given here as other plots lead to similar behavior. Figure 11 compares the landmark cranio-caudal coordinates

This article has been accepted for publication in a future issue of this journal, but has not been fully edited. Content may change prior to final publication.

IEEE TRANSACTIONS ON MEDICAL IMAGING 9

given by the experts to those obtained with method m_3 (Fig. 11a) and method (Fig. 11b) for the transformation ϕ_E, in patient 1. A Bland-Altman diagram plots the differences between two methods against their mean. For each diagram, 95% of differences will lie between the two straight line limits (or, more precisely, between $d - 1.96s$ and $d + 1.96s$, where d stands for the mean difference and s for the standard deviation). Such a representation is very helpful to identify situations where the results given by two methods are truly discordant. Table III shows the Student t-test results between each pair of methods, allowing to identify whether the TRE obtained with a method is statistically different from the TRE obtained with another method. The acceptable significance value α was set to 0.05. The p-value is a probability measure of the confidence against a null hypothesis $\mathcal{H}_0$. In the present case, hypothesis $\mathcal{H}_0$ was: "*the two methods are equivalent according to the computed TRE metric*". The lower the p-value, the more likely the difference between methods is significant.

TABLE II
TRE IN MILLIMETERS FOR EACH METHOD AT EACH TIME POINT. FOR EACH CASE, THE FIRST VALUE CORRESPONDS TO THE MEAN VALUE OF THE TRE CRITERION. THE TWO VALUES IN PARENTHESES CORRESPOND TO THE FIRST AND THIRD QUARTILES, RESPECTIVELY

Methods	Patient 1		
	ϕ_1	ϕ_2	ϕ_E
m_0	5.1 (1.8 / 7.4)	8.4 (4.3 / 10.8)	11.4 (7.6 / 15.1)
m_1	2.7 (1.1 / 4.0)	1.8 (1.1 / 2.2)	1.7 (1.0 / 2.3)
m_2	3.0 (1.2 / 3.5)	2.0 (1.0 / 2.4)	1.7 (0.9 / 2.5)
m_3	4.5 (2.3 / 5.5)	5.9 (3.0 / 7.5)	6.5 (4.5 / 7.7)
Methods	Patient 2		
	ϕ_1	ϕ_2	ϕ_E
m_0	3.9 (2.5 / 4.5)	5.8 (3.1 / 7.7)	6.8 (3.5 / 9.2)
m_1	2.2 (1.0 / 3.0)	2.5 (1.2 / 3.4)	1.8 (0.5 / 2.2)
m_2	1.8 (1.1 / 2.2)	1.8 (1.0 / 1.9)	1.6 (1.8 / 2.0)
m_3	2.8 (2.2 / 3.5)	3.8 (2.7 / 5)	5 (3.1 / 6.5)
Methods	Patient 3		
	ϕ_1	ϕ_2	ϕ_E
m_0	2.5 (1.7 / 2.9)	3.3 (2.2 / 3.8)	6.4 (4.8 / 7.7)
m_1	1.7 (1.0 / 2.4)	1.4 (0.9 / 1.7)	1.4 (0.9 / 1.8)
m_2	2.2 (1.4 / 2.8)	1.2 (0.6 / 1.7)	1.3 (0.9 / 1.5)
m_3	–	–	–

a) Patient 1. ϕ_1. b) Patient 1. ϕ_2. c) Patient 1. ϕ_E.

d) Patient 2. ϕ_1. e) Patient 2. ϕ_2. f) Patient 2. ϕ_E.

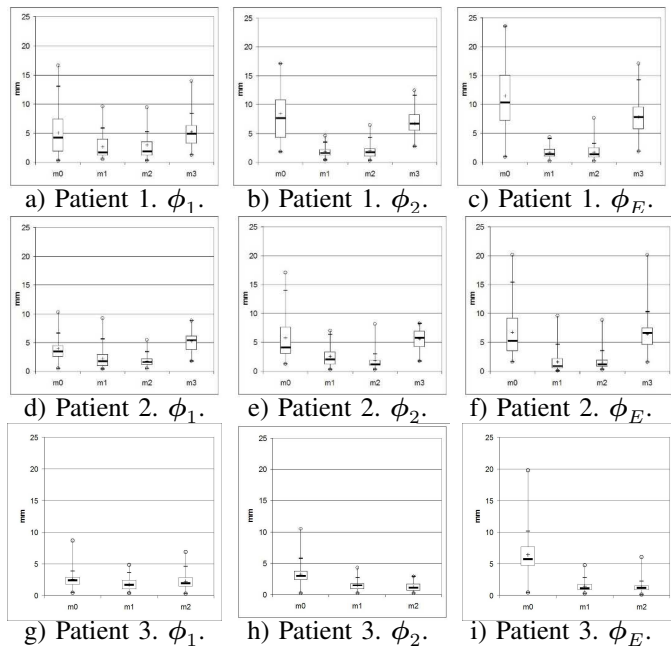g) Patient 3. ϕ_1. h) Patient 3. ϕ_2. i) Patient 3. ϕ_E.

Fig. 10. Box and Whiskers plots for the TRE criterion obtained for the motion estimation methods. The first line corresponds to patient 1, the second line to patient 2 and the third line to patient 3. First column corresponds to ϕ_1, second to ϕ_2 and third to ϕ_E. Each subfigure displays the box and whiskers plot for the four methods: m_0 is without transformation, m_1 corresponds to the bi-pyramidal free form-based image registration, m_2 to the optimized optical flow method and m_3 to the biomechanical method.

B. Second criterion : STE

Figure 12 displays the length of the ***PRT*** according to the distance to the lung apex for patient 1. The greater displacements were observed near the diaphragm. Therefore, the magnitude of the motion to be recovered by motion estimators was variable along the thorax (from about $3\,mm$ near the apex to $25\,mm$ close to the diaphragm). Table IV gives the STE statistics between the ***PRT*** and ***PET*** obtained with each method in order to discuss spatio-temporal errors.
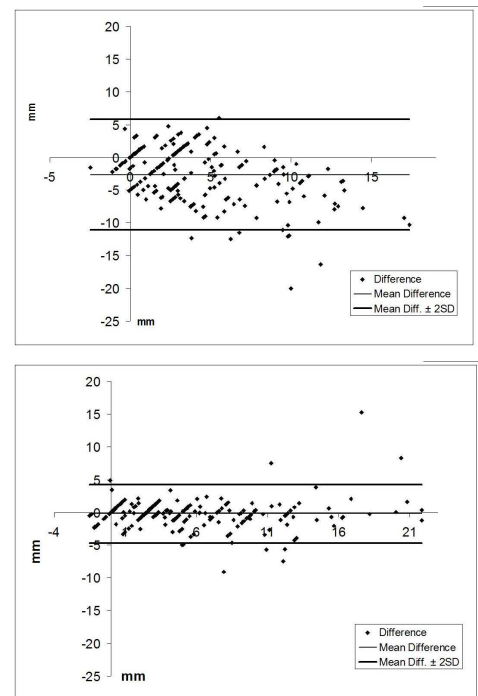

Fig. 11. Example of Bland-Altman plots for comparing motion estimation methods (transformation ϕ_E, patient 1); on top, comparison of cranio-caudal displacements: expert's reference against m_3 estimations; on botton, comparison of cranio-caudal displacements: expert's reference against m_1 estimations.

This article has been accepted for publication in a future issue of this journal, but has not been fully edited. Content may change prior to final publication.

IEEE TRANSACTIONS ON MEDICAL IMAGING 10

TABLE III
STATISTICAL TESTS PERFORMED ON EACH PAIR OF METHODS (FOR ALL
PATIENTS, ALL LANDMARKS AND ALL MOTION ESTIMATION METHODS).
IF P-VALUE IS GREATER THAN 0.1, THE DIFFERENCE IS NOT
STATISTICALLY SIGNIFICANT (SYMBOL '='). IF $p < 0.1$ THE DIFFERENCE
IS SIGNIFICANT (SYMBOL '+') AND IF $p < 0.001$, THE DIFFERENCE IS
HIGHLY SIGNIFICANT (SYMBOL '+ + +').

	Comparison	p-value	Is difference significant ?
	m_0 vs m_1	<0.0001	+++
	m_0 vs m_2	<0.0001	+++
Patient 1	m_0 vs m_3	0.00001	++
	m_1 vs m_2	0.42	=
	m_1 vs m_3	<0.0001	+++
	m_2 vs m_3	<0.0001	+++
	Comparison	p-value	Is difference significant ?
	m_0 vs m_1	<0.0001	+++
	m_0 vs m_2	<0.0001	+++
Patient 2	m_0 vs m_3	0.5067	=
	m_1 vs m_2	0.007	+
	m_1 vs m_3	<0.0001	+++
	m_2 vs m_3	<0.0001	+++
	Comparison	p-value	Is difference significant ?
	m_0 vs m_1	<0.0001	+++
Patient 3	m_0 vs m_2	<0.0001	+++
	m_1 vs m_2	0.34	=

The temporal sampling differed from one sequence to another as a function of the breathing cycle modeling (Eq. 4 and Fig. 5). The importance of accounting for motion (through intermediate time points) in radiation treatment is assessed in table V which provides the STE statistics between the **PRT** and **SET** obtained with each registration method. In particular, these results allow to discuss whether all the frames of the sequence are essential or if only a few of them (i.e. the two extreme phases) are needed. Table VI displays the results of the Student t-test comparing the STE metric obtained with **SET** and **PET**, respectively.
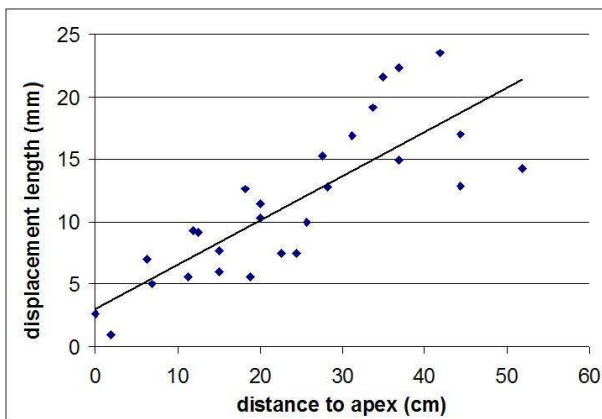

Fig. 12. Distribution of the norm of the displacements according to the distance to the lung apex for patient 1 (PRT).

TABLE V
FOR EACH SEQUENCE, STE METRIC (MEAN VALUE IN MILLIMETERS ±
STANDARD VARIATION), BETWEEN **PRT**S AND THE **SRT**S ON THE ONE
HAND AND THE **SET**S ON THE OTHER HAND. ALL LANDMARKS ARE
TAKEN INTO ACCOUNT.

Methods	STE		
	Patient 1	Patient 2	Patient 3
PRT *vs.* **SRT**	2.9 ± 1.7	1.2 ± 0.7	0.6 ± 0.2
PRT *vs.* **SET** (m_1)	3.3 ± 1.8	1.7 ± 1.1	1.0 ± 0.5
PRT *vs.* **SET** (m_2)	3.4 ± 2.0	1.7 ± 1.2	1.0 ± 0.4
PRT *vs.* **SET** (m_3)	5.6 ± 2.4	3.9 ± 1.8	–

VI. DISCUSSION

The proposed framework allows the comparison, in terms of accuracy, of motion estimation methods from 4D scans. First, the punctual accuracy of the three selected methods (m_1, m_2 and m_3) was evaluated with the TRE criterion, and the behavior of the different methods was studied with the help of statistical tools (Bland-Altman, Box and Whiskers and Student t-tests). The STE criterion introduces temporal information into the evaluation framework through a breathing model. This is to better take into account the dynamics of the organs in our context, which is of particular importance in radiotherapy of the lungs.

A. Method accuracy (TRE criterion)

Overall landmark errors (TRE, table II) for the two intensity-based methods m_1 and m_2 ($2.1\,mm$ and $2.0\,mm$, respectively) were in agreement with the voxel size ($0.9 \times 0.9 \times 2.5\,mm^3$) and the experts variability ($1.2\,mm$). We also observed that displacements were generally slightly under-estimated (mean difference of the Bland-Altman diagrams below the zero line), suggesting that the regularizations used in intensity-based methods (cubic B-splines for m_1 and Gaussian smoothing for m_2) sometimes prevent points to reach their true location. For the biomechanical method m_3, only a rather rough mesh was considered (mean hexahedron size is $24 \times 12 \times 3mm^3$ for patient 1 and $10 \times 10 \times 10mm^3$ for patient 2). The landmark points were defined in areas of significant intensity gradients which correspond to materially heterogeneous regions not yet included into the biomechanical model. Nevertheless, we observe in Fig. 10 that the estimated average error is approximately less than half the average mesh element size: lower than $6.5\,mm$ for patient 1 and lower than $5\,mm$ for patient 2. Bland-Altman diagrams (Fig. 11), revealed one specific landmark position for which the location provided by the experts was not in agreement. After discussion with the experts, this landmarks was discarded from the experiments.

The TRE statistical descriptors (mean, quartiles, Fig. 10 and table II) computed from m_1 and m_2 are similar between patient 1 and patient 2 despite the overall greater motion magnitude in patient 1 (see tab. II). The slight differences observed between m_1 and m_2 may be related to the transformation model used. The non parametric representation of method m_2 allows to estimate deformation with a precision depending on the voxel size. For method m_1, the motion field was expressed

This article has been accepted for publication in a future issue of this journal, but has not been fully edited. Content may change prior to final publication.

IEEE TRANSACTIONS ON MEDICAL IMAGING 11

TABLE IV

STE METRIC (MEAN VALUE IN MILLIMETERS $\pm$ STANDARD VARIATION), FOR THE THREE DATASETS, BETWEEN **PRT**S AND **PET**S OBTAINED WITH EACH METHOD. THE LAST THREE COLUMNS DEPICT MAXIMUM STE VALUES.

Methods	STE			Maximum STE		
	Patient 1	Patient 2	Patient 3	Patient 1	Patient 2	Patient 3
m_0 (no motion)	6.8 ± 3.6	4.2 ± 2.7	3.2 ± 1.7	14.6	11.6	9.4
m_1 (**PRT** vs **PET**)	2.2 ± 1.2	1.7 ± 0.9	1.2 ± 0.4	5.1	4.4	2.6
m_2 (**PRT** vs **PET**)	2.3 ± 1.5	1.3 ± 0.9	1.2 ± 0.5	6.5	5.7	3.4
m_3 (**PRT** vs **PET**)	5.6 ± 1.9	4.3 ± 1.4	–	10.4	8.7	–

TABLE VI

STATISTICAL TESTS PERFORMED (FOR EACH PATIENT AND EACH POINT) TO COMPARE **SET**S AND **PET**S FOR EACH METHOD. IF P-VALUE IS GREATER THAN 0.1, THE DIFFERENCE IS NOT STATISTICALLY SIGNIFICANT (SYMBOL '='). IF $p < 0.1$ THE DIFFERENCE IS SIGNIFICANT (SYMBOL '+') AND IF $p < 0.001$, THE DIFFERENCE IS VERY SIGNIFICANT (SYMBOL '+ + +').

	Comparison	p-value	Is difference significant ?
Patient 1	**SET**(m_1) vs **PET**(m_1)	<0.0001	+ + +
	SET(m_2) vs **PET**(m_2)	<0.0001	+ + +
	SET(m_3) vs **PET**(m_3)	0.63	=
	Comparison	p-value	Is difference significant ?
Patient 2	**SET**(m_1) vs **PET**(m_1)	0.95	=
	SET(m_2) vs **PET**(m_2)	<0.0001	+ + +
	SET(m_3) vs **PET**(m_3)	0.0039	+ +
	Comparison	p-value	Is difference significant ?
Patient 3	**SET**(m_1) vs **PET**(m_1)	0.0005	+ + +
	SET(m_2) vs **PET**(m_2)	<0.0001	+ + +

with a continuous model and the accuracy depended on the size of the grid and of a region of interest (ROI). For example, in patient 1 dataset, the ROI was about 200×200 pixels in the acquisition plane, corresponding to approximately one control point every 10 voxels ($9\,mm$ in native image plane). The ROI was larger for patient 2 dataset (250×250 pixels) due to morphological differences between the two patients implying a distribution of one control point every 14 voxels ($12.6\,mm$ in native image plane). This might explain accuracy differences between the two sequences when using method m_1.

Methods m_1 and m_2 were found to be statistically similar but significantly different from method m_3 ($p < 0.001$), as shown by results of the Student t-tests summed up in table III.

B. Trajectory study (STE criterion)

1) STE as a method evaluation criterion: The study of trajectories through the STE metric showed that the mean distance between reference (**PRT**) and estimated piecewise-linear trajectories (**PET**) was around $1.6\,mm$ with methods m_1 and m_2 and around $5\,mm$ with method m_3 (tab. IV). The difference between methods m_1 and m_2 was found not statistically significant. With m_1 and m_2, the STE for patient 1 (see tab. IV) was slightly higher than the mean of the three TRE (2.0 and $2.2\,mm$ compared to 2.2 and $2.3\,mm$, table II), while the STE for patients 2 and 3 were inferior to the corresponding TRE values. Even if m_1 and m_2 lead to comparable average results, the maximum STE was lower using method m_1. Whereas each time point contributes with an equal weight to the mean TRE, STE metric introduces a variable weight according to the breathing cycle model and

displacement speed along the trajectories. This implies that intermediate time points (ϕ_1 and ϕ_2) influence depends on their relative location in the breathing cycle (see Fig. 5). STE values are inferior to the mean TRE values for patients 2 and 3 ($1.7/1.2\,mm$ vs $2.2/1.5\,mm$ average TRE for method m_1) because most influent time point is t_E. On the contrary, STE values are greater to the mean TRE values for patient 1 since first intermediate time point contributes more. In conclusion, STE metric takes into account the breathing dynamics and the acquisition time of each of the sequence frame.

The STE criterion depends on the selected breathing model. Other breathing models could be considered. The proposed framework could also be used to study the hysteresis pattern which is known to occur during breathing (different inhalation and exhalation pathways), but it would require the definition of many more landmarks. STE criteria should be well adapted to compare inhalation and exhalation trajectories and to put the focus on different parts of the breathing cycle.

2) Taking intermediate frames into account in lung radiotherapy treatments: Table V illustrates, through the three sequences studied, the importance of taking into account motion in radiotherapy treatment. **PRT** compared to **SRT** represents the error committed when straight-linear trajectories are considered instead of piecewise-linear ones. This error was particularly low for patients 2 and 3 ($1.2\,mm$ and $0.6\,mm$, respectively). It suggests that, for the considered trajectories, the observed motion was almost rectilinear. Indeed, using straight-linear trajectories (one single motion estimation between end-inspiration and end-expiration images) increased the overall error for patient 1 whereas errors remain almost

This article has been accepted for publication in a future issue of this journal, but has not been fully edited. Content may change prior to final publication.

IEEE TRANSACTIONS ON MEDICAL IMAGING
12

equivalent for patients 2 and 3 (in Tab. IV and V, STE rises from 2.2 to $3.3\,mm$ for method m_1). However, it is not clear at this stage whether such discrepancies in accuracy results between patients come from the variablity in patient organ motion or from the 4D acquisitions. Moreover, methods behave differently: although results for m_1 and m_2 lead to similar STE, table VI shows that the error difference between straight-linear and piecewise-linear trajectories was highly significant for method m_2 for all patient whereas, for method m_1 it was significant for patient 1 and 3. It seems that trajectories estimated with method m_1 were more linear than those estimated with method m_2. The results concerning method m_3 called our attention to the contact conditions of the Finite Element Model. We observed afterward that this contact condition had not been properly handled. In particular, the conditions for surface contact had not been met for some nodes due to the mesh resolution, thus explaining why some differences could be observed. Inaccuracy at the contact was of the order of $5\,mm$, which explains why the differences were almost constant, whatever the displacement, and why the straight-linear process gave better results. Moreover, even if the method m_3 is still under development, the current evaluation study has made it possible to point out some of the problems that should be solved in the future. Overall, the benefit of incorporating additional frames for taking into account the breathing motion appears to depend on the patient. So, in the abscence of *a priori* information on the patient breathing pattern, it is certainly better to dispose of more than the two extreme phase images.

Criteria were computed over the whole image domain. But it is known that lung motion is not homogeneous during the breathing cycle and that trajectories are longer and more linear near the diaphragm than near the lung apex (Fig. 12). In the future, by using the same criteria, it should be very interesting to study motion behavior in the different parts of the lungs (lower part of the lung versus upper part, tumor areas). The chronology of the landmark trajectory is globally imposed by the Lujan's model : all the landmarks are assumed to have the same temporal evolution (homogeneous behaviour), but it is known that such an assumption is not rigorously true. However, if information about the breathing pattern in different lung regions would be available (for example by means of external or internal markers), it could be easily inserted into the proposed STE measure : currently $V(t)$ only depends on the time variable, it would switch to $V(\mathbf{x}, t)$ according to a spatio-temporal breathing model. Indeed, the main reason for using a breathing model is to compensate for the limited number of temporal frames. The model would be less necessary if we dispose of more temporally resolved sequences. However, there is still a tradeoff between image spatial and temporal resolutions and the acquisition costs in terms of dose delivered to the patient, the compatibility of the acquisition time with the clinical constraints and the management of large amounts of data. The acquisitions considered in this paper take into account those constraints as they have been indeed used for patient treatment planning.

Motion validation by means of landmarks is intrinsically limited to the point location with the consequence that no information is available in between those points. Landmarks were selected as evenly as possible all over the lungs based on visible anatomical structures. However in homogeneous regions, no landmark could be identified and thus the quality of the estimated deformation field could no be assessed within these regions. Moreover, medical experts generally find it difficult and time consuming to select landmarks . This is the reason why the number of landmarks was limited to some tens. To our knowledge, this is one of the first time that such an evaluation is performed on the lungs with such a significant number of landmarks. More complex primitives (such as 3D lines following vessels) would bring higher level information and thus contribute to define a better ground truth for the evaluation. This would still require to be evaluated by experts which is a difficult task in 3D.

VII. CONCLUSION

In this paper, we propose a strategy and criteria in order to evaluate the accuracy of motion estimators from 4D CT sequences with a limited number of phases between end-inspiration and end-expiration. Such an evaluation is particularly crucial in radiation therapy where estimated motion can be used to estimate the distribution of the absorbed dose during the therapeutic irradiation of moving organs such as the lungs. The main contributions of this paper were the setup of test cases and of a procedure to obtain expert inputs (carefully identifying more than 500 landmarks over 4 phases and 3 patients) and the proposal of spatio-temporal criteria to evaluate the predictions of landmark displacements through the respiratory cycle. The spatio-temporal trajectory error (STE) criterion allows to take into account the dynamics of the motion by introducing an *a priori* respiratory cycle modeling. It can be considered as a specialization of the TRE metric to the specific context of breathing motion compensation. The proposed comparison framework was illustrated by the study of three different motion estimation methods (two registration based methods, and one biomechanical model based method). The study allowed to compare the accuracy of those methods and to highlight some of their limits. The analysis also demonstrated the interest of incorporating several frames over the respiratory cycle in view to better adapt the therapy of lung tumors to the patient. This study has been conducted on three 4D datasets encompassing only half the respiratory cycle. The study should be pursued by including additional datasets and extending the tracking over the entire respiratory cycle. Adding more landmarks, in particular outside the lung region, could also improve the evaluation of accuracy. Dose deposit simulations could be performed on 4D images in order to quantify the influence of the type of motion estimators on dose distribution. Finally, a similar framework could also be used to evaluate motion tracking methods in other medical imaging contexts such as in cardiac motion analysis.

REFERENCES

[1] M. Goitein, "Organ and tumor motion: An overview," *Seminars in Radiation Oncology*, vol. 14, no. 1, pp. 2–9, Jan. 2004.

[2] C. Ling, E. Yorke, H. Amols, J. Mechalakos, Y. Erdi, S. Leibel, K. Rosenzweig, and A. Jackson, "Editorial : high-tech will improve radiotherapy of NSCLC: a hypothesis waiting to be validated," *International Journal of Radiation Oncology Biology Physics*, vol. 60, no. 1, pp. 3–7, 2004.

[3] G. Mageras and E. Yorke, "Deep inspiration breath hold and respiratory gating strategies for reducing organ motion in radiation treatment," *Seminars in Radiation Oncology*, vol. 14, no. 1, pp. 65–75, Jan. 2004.

[4] S. Vedam, P. Keall, V. Kini, H. Mostafavi, H. Shukla, and R. Mohan, "Acquiring a four-dimensional computed tomography dataset using an external respiratory signal," *Physics in Medecine and Biology*, vol. 48, no. 1, pp. 45–62, 2003.

[5] P. Keall, S. Joshi, S. Vedam, J. Siebers, V. Kini, and R. Mohan, "Four-dimensional radiotherapy planning for DMLC-based respiratory motion tracking," *Medical physics*, vol. 32, no. 4, pp. 942–951, 2005.

[6] T. Zhang, R. Jeraj, H. Keller, W. Lu, O. GH., M. TR., T. Mackie, and P. B., "Treatment plan optimization incorporating respiratory motion," *Medical physics*, vol. 31, no. 6, pp. 1576–86, June 2004.

[7] E. Rietzel, G. Chen, N. Choi, and C. Willet, "Four-dimensional image-based treatment planning: Target volume segmentation and dose calculation in the presence of respiratory motion," *International Journal of Radiation Oncology Biology Physics*, vol. 61, no. 5, pp. 1535–50, Apr. 2005.

[8] K. Brock, M. DL., T. H. RK., H. SJ., L. Dawson, and J. Balter, "Inclusion of organ deformation in dose calculations," *Medical physics*, vol. 30, no. 3, pp. 290–5, Mar. 2003.

[9] J. West, J. Fitzpatrick, M. Wang, B. Dawant, C. Maurer, R. Kessler, R. Maciunas, C. Barillot, D. Lemoine, A. Collignon, F. Maes, P. Suetens, D. Vandermeulen, P. Elsen, S. Napel, T. Sumanaweera, B. Harkness, P. Hemler, D. Hill, D. Hawkes, C. Studholme, J. Maintz, M. Viergever, G. Malandain, X. Pennec, M. Noz, G. Maguire, M. Pollack, C. Pelizzari, R. Robb, D. Hanson, and R. Woods, "Comparison and Evaluation of Retrospective Intermodality Image Registration Techniques," *Journal of Computed Assisted Tomography*, vol. 21, no. 4, pp. 554–566, 1997.

[10] J. Fitzpatrick and J. West, "The distribution of target registration error in rigid-body point-based registration," *IEEE Trans. Med. Imag.*, vol. 20, no. 9, pp. 917–927, Sept. 2001.

[11] N. Pauna, P. Croisille, N. Costes, A. Reilhac, T. Makela, O. Cozar, M. Janier, and P. Clarysse, "A strategy to quantitatively evaluate MRI/PET cardiac rigid registration methods using a Monte Carlo simulator," in *Springer LNCS 2674, Proceedings of FIMH'03 (Second International Workshop on functional Imaging and Modeling of the Heart)*, Lyon France, 2003, pp. 194–204.

[12] P. Hellier, C. Barillot, I. Corouge, B. Gibaud, G. L. Goualher, D. L. Collins, A. Evans, G. Malandain, N. Ayache, G. E. Christensen, and H. J. Johnson, "Retrospective evaluation of intersubject brain registration," *IEEE Trans. Med. Imag.*, vol. 22, no. 9, pp. 1120–1130, Sept. 2003.

[13] T. Pan, T. Lee, E. Rietzel, and G. Chen, "4D-CT imaging of a volume influenced by respiratory motion on multi-slice CT," *Medical physics*, vol. 31, no. 2, pp. 333–340, 2004.

[14] D. Sarrut, V. Boldea, M. Ayadi, J. Badel, C. Ginestet, and S. Clippe, "Non-rigid registration method to assess reproducibility of breath-holding with ABC in lung cancer," *International Journal of Radiation Oncology Biology Physics*, vol. 61, no. 2, pp. 594–607, 2005.

[15] J. W. Tukey, "Box-and-Whisker Plots," *Exploratory Data Analysis*, pp. 39–43, 1977.

[16] J. Bland and D. Altman, "Statistical methods for assessing agreement between two methods of clinical measurement," *Lancet*, vol. 1, pp. 307–310, 1986.

[17] A. Lujan, L. EW, J. Balter, and R. Ten Haken, "A method for incorporating organ motion due to breathing into 3D dose calculations," *Medical physics*, vol. 26, no. 5, pp. 715–20, 1999.

[18] R. George, S. Vedam, T. Chung, V. Ramakrishnan, and P. J. Keall, "The application of the sinusoidal model to lung cancer patient respiratory motion," *Medical physics*, vol. 32, no. 9, pp. 2850–2861, Sept. 2005.

[19] W. Crum, T. Hartkens, and D. Hill, "Non-rigid image registration: theory and practice," *Br J Radiol.*, vol. 77, no. 2, pp. 140–153, 2004.

[20] B. Zitova and J. Flusser, "Image registration methods: a survey," *Image and Vision Computing*, vol. 21, pp. 977–1000, 2003.

[21] C. Maurer and J. Fitzpatrick, "A review of medical image registration," *In Interactive ImageGuided Neurosurgery, R. J. Maciunas, Ed. American Association of Neurological Surgeons, Park Ridge, IL,*, pp. 17–44, 1993.

[22] L. Fan, C. Chen, J. Reinhardt, and E. Hoffman, "Evaluation and application of 3D lung warping and registration model using HRCT images," in *SPIE Medical Imaging*, vol. 4321, San Diego, CA, 2001, pp. 234–243.

[23] B. Li, G. Christensen, E. Hoffman, G. McLennan, and J. Reinhardt, "Establishing a normative atlas of the human lung: intersubject warping and registration of volumetric CT images," *Acad. Radiol.*, vol. 10, no. 3, pp. 255–265, 2003.

[24] D. Yan, D. Jaffray, and J. Wong, "A model to accumulate fractionated dose in a deforming organ," *International Journal of Radiation Oncology Biology Physics*, vol. 44, no. 3, pp. 665–75, June 1999.

[25] B. Schaly, J. Kempe, G. Bauman, J. Battista, and J. Van Dyk, "Tracking the dose distribution in radiation therapy by accounting for variable anatomy," *Physics in Medecine and Biology*, vol. 49, no. 5, pp. 791–805, Mar. 2004.

[26] W. Lu, M. Chen, G. Olivera, K. Ruchala, and T. Mackie, "Fast free-form deformable registration via calculus of variations," *Physics in Medecine and Biology*, vol. 49, no. 14, pp. 3067–3087, 2004.

[27] T. Sundaram and J. Gee, "Towards a model of lung biomechanics: pulmonary kinematics via registration of serial lung images," *Medical Image Analysis*, vol. 9, no. 6, pp. 254–37, Dec. 2005.

[28] M. Birkner, D. Yan, M. Alber, J. Liang, and F. Nusslin, "Adapting inverse planning to patient and organ geometrical variation: algorithm and implementation," *Medical physics*, vol. 30, no. 10, pp. 2822–31, Oct. 2003.

[29] J. Lian, L. Xing, S. Hunjan, C. Dumoulin, J. Levin, A. Lo, R. Watkins, K. Rohling, R. Giaquinto, D. Kim, D. Spielman, and B. Daniel, "Mapping of the prostate in endorectal coil-based MRI/MRSI and CT: a deformable registration and validation study," *Medical physics*, vol. 31, no. 11, pp. 3087–3094, July 2003.

[30] T. Zhang, N. Orton, T. Mackie, and B. Paliwal, "Technical note: A novel boundary condition using contact elements for finite element based deformable image registration," *Medical physics*, vol. 31, no. 9, pp. 2412–5, Sept. 2004.

[31] B. Delhay, "Estimation spatio-temporelle de mouvement et suivi de structures déformables. Application l'imagerie dynamique du coeur et du thorax," Ph.D. dissertation, Institut National des Sciences appliques de Lyon, 2006.

[32] B. Delhay, P. Clarysse, C. Pera, and I. E. Magnin, "A spatio-temporal deformation model for dense motion estimation in periodic cardiac image sequences," in *Workshop MICCAI 2006 : From Statistical Atlases to Personalized Models : Understanding Complex Diseases in Populations and Individuals.*, Copenhage Denmark, 2006, pp. 87–90.

[33] T. W. Sederberg and S. R. Parry, "Free-Form Deformation of solid geometric models," *Proceedings of SIGGRAPH 86, Computer Graphics 20*, vol. 4, pp. 151–159, August 1986.

[34] D. Rueckert, L. I. Sonoda, C. Hayes, D. L. Hill, M. O. Leach, and D. J. Hawkes, "Nonrigid registration using Free-Form Deformations: application to breast MR images." *IEEE Trans. Med. Imag.*, vol. 18, no. 8, pp. 712–721, August 1999.

[35] M. J. Ledesma-Carbayo, J. Kybic, M. Desco, A. Santos, M. Shuling, and P. H. ans M. Unser, "Spatio-temporal nonrigid registration for ultrasound cardiac motion estimation," *IEEE Trans. Med. Imag.*, vol. 24, no. 9, pp. 1113–1126, Sept 2005.

[36] V. Noblet, C. Heinrich, F. Heitz, and J. Armspach, "3-D deformable image registration: a topology preservation scheme based on hierarchical deformation models and interval analysis optimization," *IEEE Trans. Image Processing*, vol. 14, no. 5, pp. 553–566, May 2005.

[37] T. Rohlfing, C. Maurer, D. Bluemke, and M. Jacobs, "Volume-preserving non-rigid registration of MR breast images using free-form deformation with an incompressibility constraint," *IEEE Trans. Med. Imag.*, vol. 22, no. 6, pp. 730–741, June 2003.

[38] S. Lee, G. Wolberg, and S. Y. Shin, "Scattered data interpolation with multilevel B-Splines," *IEEE Trans. Visual. Comput. Graphics*, vol. 3, no. 3, pp. 228–244, 1997.

This article has been accepted for publication in a future issue of this journal, but has not been fully edited. Content may change prior to final publication.

IEEE TRANSACTIONS ON MEDICAL IMAGING

14

[39] D. Sarrut, V. Boldea, S. Miguet, and C. Ginestet, "Simulation of 4D CT images from deformable registration between inhale and exhale breath-hold CT scans," *Medical physics*, 2006, to appear.

[40] V. Boldea, D. Sarrut, and S. Clippe, "Lung deformation estimation with non-rigid registration for radiotherapy treatment," in *Medical Image Computing and Computer-Assisted Intervention MICCAI'2003*, vol. 2878. Springer Verlag, Lecture Notes in Computer Science, 2003, pp. 770–7.

[41] V. Boldea, D. Sarrut, and C. Carrie, "Comparison of 3D dense deformable registration methods for breath-hold reproducibility study in radiotherapy," in *SPIE Medical Imaging: Visualization, Image-Guided Procedures, and Display*, vol. 5747, 2005, pp. 222–230.

[42] J. Thirion, "Image matching as a diffusion process: an analogy with Maxwell's demons," *Medical Image Analysis*, vol. 2, no. 3, pp. 243–260, 1998.

[43] X. Pennec, P. Cachier, and N. Ayache, "Understanding the demon's algorithm: 3D non rigid registration by gradient descent," in *Medical Image Computing and Computer-Assisted Intervention MICCAI'99*, C. Taylor and A. Colschester, Eds., vol. 1679. Cambridge, UK: Springer Verlag, Lecture Notes in Computer Science, 1999, pp. 597–605.

[44] P. Cachier and N. Ayache, "Isotropic energies, filters and splines for vectorial regularization," *J. of Math. Imaging and Vision*, vol. 20, no. 3, pp. 251–265, May 2004.

[45] R. Deriche, "Recursively implementing the gaussian and its derivatives," INRIA, Tech. Rep. 1893, Apr. 1993, http://www.inria.fr/rrrt/rr-1893.html.

[46] Q. Grimal, A. Watzky, and S. Naili, "Nonpenetrating impact on the thorax : a study of the wave propagation," *Comptes Rendus de l'Academie des Sciences*, vol. IIb, no. 329, pp. 655–662, 2001.

[47] K. Brock, M. Sharpe, L. Dawson, S. Kim, and D. Jaffray, "Accuracy of finite element model-based multi-organ deformable image registration," *Medical physics*, vol. 32, no. 6, pp. 1647–59, June 2005.

[48] P. Villard, M. Beuve, B. Shariat, V. Baudet, and F. Jaillet, "Simulation of lung behaviour with finite elements: Influence of bio-mechanical parameters," in *MEDIVIS '05: Proceedings of the Third International Conference on Medical Information Visualisation–BioMedical Visualisation*. Washington, DC, USA: IEEE Computer Society, 2005, pp. 9–14.

[49] W. Lorensen and H. Cline, "Marching cubes: a high resolution 3D surface reconstruction algorithm," *Computer Graphics*, vol. 21, pp. 163–169, 1987.

[50] P. Villard, M. Beuve, B. Shariat, V. Baudet, and F. Jaillet, "Lung mesh generation to simulate breathing motion with a finite element method," in *Information Visualisation*. London, GB: IEEE Computer Society, 2004, pp. 194–199.

[51] M. L. Moy and S. H. Loring, "Compliance," *Seminar in respiratory and critical care medecine*, vol. 19, no. 4, pp. 349–359, 1998.

[52] J. Humphrey, "A possible role of the pleura in lung mechanics," *J Biomech*, vol. 20, no. 8, pp. 773–777, 1987.

[53] O. C. Zienkiewicz and R. L. Taylor, *The finite element method*, 5th ed. Butterworth-Heinemann, 2000.

[54] J. Simo and C. Miehe, "Associative coupled thermoplasticity at finite strains: formulation, numerical analysis and implementation," *Comp. Meth. Appl. Mech. Eng.*, vol. 98, pp. 41–104, 1992.

Bertrand Delhay Bertrand Delhay was born in 1979. He received in 2003 the M.S degree in Electrical engineering and Image Processing and in 2007 a Ph.D. in Medical Image Processing from the Institut National des Sciences Appliquées (INSA) of Lyon, France. He is currently a Researcher at the Center for Research and Applications in Image and Signal Processing (CREATIS). His research interests include signal and image processing and more particularly motion estimation and structure tracking applied to CT or MR image sequences.

Pierre-Frédéric Villard Pierre-Frederic Villard is a post-doctorate fellow at the University Claude Bernard Lyon 1. He received his PhD from the University Claude Bernard Lyon 1 in 2006. His research interests include computer graphics, finite element methods, soft object deformation modeling and medical images processing.

Vlad Boldea Vlad Boldea graduated in computer science from the Université Claude Bernard Lyon 1, France in 2001. He obtained the M.S. degree (DEA Images et Systemes) from the Institut National des Sciences Appliquées (INSA) of Lyon, France in 2002, and a Ph.D. in Computer Science from the Université Lumière Lyon 2, France in 2006. He currently holds a post-doctoral position at Laboratoire d'InfoRmatique en Images et Systèmes d'information (LIRIS), in Lyon, France, and his research is done in collaboration with the Radiotherapy Department of Léon Bérard cancer center. His research areas of interest are the estimation and analysis of organ motion and deformation from different image modalities.

David Sarrut Born in 1974, David Sarrut received a PhD in computer science in 2000. Initially assistant professor, he is now a researcher at Léon Bérard cancer center. He is a member of the Center for Research and Applications in Image and Signal Processing (CREATIS). His principal domain of interests is image analysis and processing applied to radiotherapy and hadrontherapy.

Michael Beuve After studying engineering at the Ecole Centrale de Lyon, Michael did my Ph-D at the Centre Interdisciplinaire de Recherche Ion Laser (Caen-France) on the Monte Carlo simulation of the electronic processes induced in material by ion irradiation. In 1999, he studied the specific effects of high-LET radiations at the Centro Atomico Bariloche (Argentina). Both at the Gesellschaft fr Schwerionenforschung (Darmstadt-Germany) and at the Hahn Meitner Institut (Berlin-Germany), he developed a simulation of damages induced by ion irradiation. Since 2001, he is associate professor in computing science and physics at the University of Lyon, working on cancer treatment by hadrontherapy (radiobiology effects of ion irradiation and modeling organ motions for an accurate tumor targeting).

This article has been accepted for publication in a future issue of this journal, but has not been fully edited. Content may change prior to final publication.

IEEE TRANSACTIONS ON MEDICAL IMAGING 15

Patrick Clarysse Patrick Clarysse received the MD degree in 1987 and a PhD in 1991 from the Scientific and Technological University of Lille, France. Since 1992, Patrick Clarysse has been working with the French National Center for Scientific Research (CNRS) at CREATIS, CNRS UMR 5220, Inserm U630, Lyon, France. His primary research interests are in bioengineering and medical image analysis, and include multimodal image segmentation and registration, motion estimation and deformable models with applications to the analysis of heart functions and the motion of thoracic structures.